Industrial Kraft Lignin Based Binary Cathode Interface Layer Enables Enhanced Stability in High Efficiency Organic Solar Cells

Zhang, Qilun; Liu, Tiefeng; Wilken, Sebastian; Xiong, Shaobing; Zhang, Huotian; Ribca, Iuliana; Liao, Mingna; Liu, Xianjie; Kroon, Renee; Fabiano, Simone; Gao, Feng; Lawoko, Martin; Bao, Qinye; Österbacka, Ronald; Johansson, Mats; Fahlman, Mats

Industrial Kraft Lignin Based Binary Cathode Interface Layer Enables Enhanced Stability in High Efficiency Organic Solar Cells

Qilun Zhang,* Tiefeng Liu, Sebastian Wilken, Shaobing Xiong, Huotian Zhang, Iuliana Ribca, Mingna Liao, Xianjie Liu, Renee Kroon, Simone Fabiano, Feng Gao, Martin Lawoko, Qinye Bao,* Ronald Österbacka, Mats Johansson, and Mats Fahlman*

Herein, a binary cathode interface layer (CIL) strategy based on the industrial solvent fractionated LignoBoost kraft lignin (KL) is adopted for fabrication of organic solar cells (OSCs). The uniformly distributed phenol moieties in KL enable it to easily form hydrogen bonds with commonly used CIL materials, i.e., bathocuproine (BCP) and PFN-Br, resulting in binary CILs with tunable work function (WF). This work shows that the binary CILs work well in OSCs with large KL ratio compatibility, exhibiting equivalent or even higher efficiency to the traditional CILs in state of art OSCs. In addition, the combination of KL and BCP significantly enhanced OSC stability, owing to KL blocking the reaction between BCP and nonfullerene acceptors (NFAs). This work provides a simple and effective way to achieve high-efficient OSCs with better stability and sustainability by using wood-based materials.

1. Introduction

In an effort to meet the ever increasing energy demand of human civilization with renewable, clean, and sustainable solar energy, organic solar cells (OSCs) have drawn increasing scientific interest owing to their unique advantages for application in flexible and portable devices such as low cost, light weight, and large area printable fabrication.[1–4] Benefiting from the rapid development in novel organic photoactive materials, especially in fused ring electron acceptors (FREAs) which have low energy loss and high absorbance coefficient, the power conversion efficiency of single junction OSCs has surpassed 19%.[5–9]

As a critical constituent in OSCs, the cathode interface layer (CIL) plays a vital role in improving the PCE and stability in devices.[10–12] A suitable CIL between the active layer and metal cathode can effectively create Ohmic contact formation, tune the energy level alignment, and improve the charge extraction and selection at the interface.[13–16] The properties of the CIL for state-of-art OSCs demand several stringent selection criteria. Firstly, a deep lowest unoccupied molecular orbital (LUMO) energy of the FREAs proposes new challenges in obtaining energy level alignment that favors charge extraction and selection at the metal-organic interface.[17–19] Secondly, chemical inertness between the FREA and CIL is needed, as the strong

Q. Zhang, T. Liu, M. Liao, X. Liu, R. Kroon, S. Fabiano, M. Fahlman
Laboratory of Organic Electronics
Department of Science and Technology (ITN)
Linköping University
Norrköping SE-60174, Sweden
E-mail: qilun.zhang@liu.se; mafah@ifm.liu.se
Q. Zhang, M. Liao, R. Kroon, S. Fabiano, M. Fahlman
Wallenberg Wood Science Center
Department of Science and Technology (ITN)
Linköping University
Norrköping SE-60174, Sweden

S. Wilken, R. Österbacka
Faculty of Science and Engineering
Åbo Akademi University
Turku 20500, Finland
S. Xiong, Q. Bao
School of Physics and Electronic Science
East China Normal University
Shanghai 200241, China
E-mail: qybao@clpm.ecnu.edu.cn
H. Zhang, F. Gao
Department of Physics
Chemistry and Biology (IFM)
Linköping University
Linköping SE-58183, Sweden
I. Ribca, M. Lawoko, M. Johansson
Department of Fiber and Polymer Technology
School of Engineering Sciences in Chemistry
Biotechnology and Health
KTH Royal Institute of Technology
Stockholm SE- 10044, Sweden

**ADVANCED
SCIENCE NEWS**

www.advancedsciencenews.com

**ADVANCED
MATERIALS**

www.advmat.de

electron-deficient characteristic of exocyclic vinyl groups (C = C) in the conjugated bridges that link donor moieties with acceptor moieties in FREAs promotes detrimental reactions with low work function CILs, such as polyethylenimine (PEI) and polyethylenimine ethoxylated (PEIE).[20–22] To address these issues, new materials are constantly developed for effective CILs, including PFN series conjugated polyelectrolytes,[15] naphthalene diimides (NDIs) and perylene diimides (PDIs).[14,23–25] An alternative approach is the use of binary CILs, where a material blend can enhance the advantages and/or passivate the weaknesses of the constituent materials.[26,27] Inclusion of biomass-derived materials is desirable and serving as one of the component in the binary CILs to enhance performance and stability is one intriguing possibility due to their unique, yet readily available chemical functionalities. Biomass-derived materials successfully have been used to stabilize photoactive layers in both perovskite[28–30] and organic solar cells.[31]

Lignin, derived from lignocellulosic biomass, is the most abundant natural source of aromatic material constituents.[32] Its phenolic as well as aliphatic hydroxyl functionalities can be used to promote intricate intermixing and interlocking of binary systems through hydrogen bonding.[33–35] Using this approach, sulfonated lignin and its derivatives were successfully combined with poly(3,4-ethylenedioxythiophene) (PEDOT) and applied as the hole transport layer in fullerene based OSCs and perovskite solar cells.[36–39] More recently, Ouyang et al. reported a chemically modified kraft lignin (KL) with more phenol and conjugated linkages as a 3D network host for PDIN, and the binary CIL showed excellent electron extraction performance in nonfullerene acceptor (NFA) OSCs.[40] Utilization of lignin as a raw material is not, however, a trivial task. Industrial lignin is heterogeneous in both structure and polydispersity, owing to the harsh physical and chemical conditions of the Kraft process which is the most commonly used process for separating lignin from biomass.[33,41,42] Thus, the potential of solvent fractionated LignoBoost KL as the host in binary CILs deserves to be explored.[43,44] The use of sequential fractionation of the soluble fractions ensures KL with suitable solvent compatibility and low polydispersity in molecular segments.

In this work, we explored the potential of methanol-soluble industrial KL (KL_{MeOH}) which was obtained via facile solvent fractionation, as the host in binary CILs. We show that the WF of the $BCP:KL_{MeOH}$ binary films can be linearly tuned by blending the two components in different ratios. Based on the binary strategy, we successfully developed CILs with efficient electron extraction ability for NFA OSCs with PM6:Y6 as the photoactive layer. We demonstrate that the binary CIL of $BCP:KL_{MeOH}$ significantly improves the stability compared to neat BCP CILs in Y6 based OSCs, due to KL-induced passivation of the strong chemical reactions between Y6 and BCP at the interface between the binary CIL and the active layer, as shown by photoelectron spectroscopy and morphology characterization. We further used the binary CIL strategy in ternary photoactive layer systems based on "Y" series NFAs, resulting in more stable OSCs and with the PCE surpassing 18% in $D18\text{-}Cl:N3:PC_{60}BM$ systems. In addition to BCP, we extend the binary CIL strategy with other traditional CIL materials, in which we can obtain similar OSC performance by using considerable KL ratio. Our results demonstrate that the binary CIL strategy based on industrial KL is a promising way to increase photovoltaic efficiency, enhance the device stability, and improve sustainability of NFA-based OSCs.
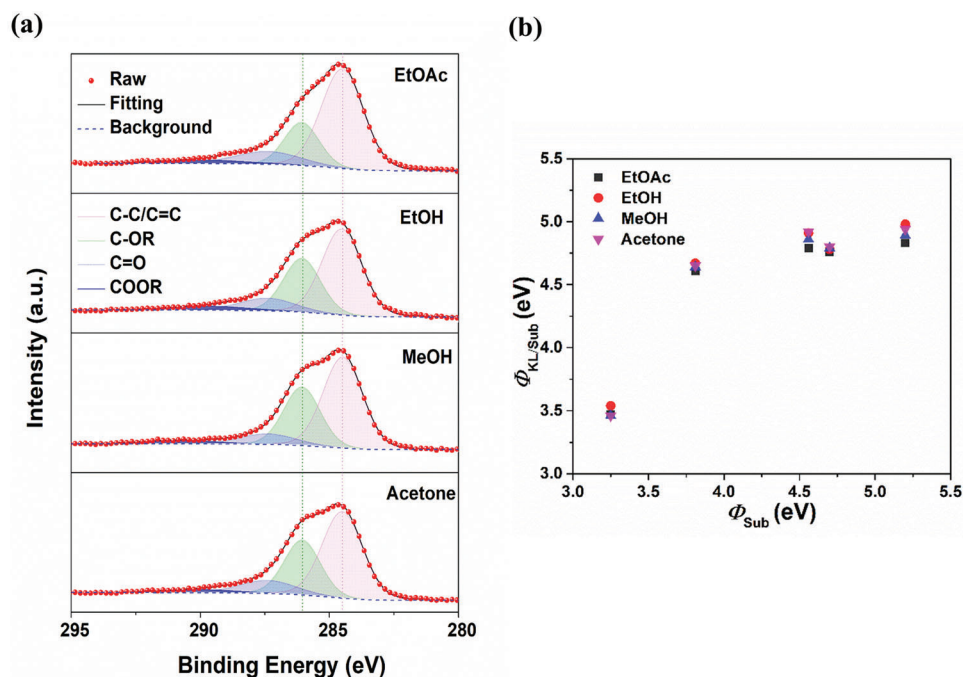
2. Results and Discussion

2.1. Preparation and Characterization of KL Based CILs

Industrial lignin (LignoBoost KL) was subjected to sequential solvent fractionation in the order of ethyl acetate (EtOAc), ethanol (EtOH), methanol (MeOH), and acetone was performed to obtain the KL fractions. The typical relative fraction mass distribution and molecular structures[34] are shown Figure S1a (Supporting Information) (reproduce from the references with permission).[35] The spin-coated thin films of these fractions follow the increasing molecular mass of each fraction, which is positive correlation to the XPS C1s core level spectra and the atomic force microscopy (AFM) images (**Figure 1**a and Figure S1b, Supporting Information). With the fractionation order, the fitted C1s core level spectra show an increasing peak feature (dark green) at about 286 eV assigned to the common linkages with the structure of C–OR, meaning more complete structure of KLs in the latter solvent fractions (the lower figures). The AFM images show an increasing R_q in general following the order EtOAc, EtOH, MeOH, and acetone, the close R_q values between the MeOH and EtOH fractions are due to the similar molecular mass. Although the films of different KL fractions show different morphology, the WF of the films on different substrates show very small differences between the fractions. The WF results are shown in Figure 1b (UPS spectra are shown in Figure S2, Supporting Information), KLs always result in the WF in the range of 4.7–4.9 eV except for the very low WF substrates.

Considering the relatively low charge mobility and mismatched WF of KL compared with commonly used OSC materials, we follow the binary CIL strategy to explore the application of the KLs based CILs to modify the metal cathode in OSCs. The alcohol moieties in KL enable it to hydrogen bond to tertiary amines, a common functional group in traditional CIL materials such as BCP (chemical structures see **Figure 2**a). BCP, a classic and effective electron transport material, is considered as the first choice as the other component to obtain the binary CIL, since it is widely used as the CILs in organic light-emitting diodes (OLEDs),[45,46] perovskite solar cells,[47,48] and fullerene based OSCs.[49,50] However, such classic material is rarely reported in state of art OSCs due to the poor stability when used with FREA-type NFAs, which are the top performing acceptors in OSCs.[51] To obtain suitably solution-processable binary CIL materials for OSCs, we use the methanol fraction KL (KL_{MeOH}) combined with the BCP. The morphology evolution of the $BCP:KL_{MeOH}$ films with increasing KL_{MeOH} ratio are shown in Figure S3 (Supporting Information), the AFM images (top) show smoother surface topology after blending BCP with KL in different ratios, whereas the SEM images (bottom) depict a obvious change from pure BCP to $BCP:KL_{MeOH}$ in the large scale, which are in consistent with the AFM images. It is noted that the molecular orientation of BCP film is amorphous, unaffected by the variation of the binary CIL morphology (see Figure S4, Supporting Information).

We used XPS for in-depth study of the interaction between each component in the CILs. The binary CILs (50% of KL_{MeOH} in mass ratio) were characterized by XPS as shown in the

**ADVANCED
SCIENCE NEWS**

www.advancedsciencenews.com

**ADVANCED
MATERIALS**

www.advmat.de

Figure 1. a) The XPS C1s core level spectra of solvent fractionated kraft lignin (KL). b) Summarized work function (WF) evaluation of solvent fractionated KL films on different substrates.

fitted N1s core level spectra in Figure 2b. The main N1s peak features at about 398.6 eV refer to the phenanthroline N (C – N = C) of BCP. In the binary films, the additional KL_{MeOH} caused a shift of the main N1s peak from 398.6 to 399 eV and a weak peak feature appears at 401.5 eV, whereas no shift of the C1s peak at ≈285 eV for the two films occurred (Figure S5a, Supporting Information). The result indicates reduction of the electron densities on the nitrogen atoms, which implies the formation of hydrogen bonding between KL_{MeOH} and BCP due to the charge transfer between phenanthroline and phenol groups. Ultraviolet photoelectron spectroscopy (UPS) was used on the $BCP:KL_{MeOH}$ binary films to explore the WF (Figure S5b, Supporting Information). The summarized ratio-dependent WF of the binary films, shown in Figure 2c, indicates that the WF of $BCP:KL_{MeOH}$ is tunable. Specifically, the WF of $BCP:KL_{MeOH}$ can be positively tuned from 3.80 to 4.85 eV by increasing the KL_{MeOH} ratio. We note that the WF of the binary CILs is less than 4.1 eV up to KL_{MeOH} ratios of 50%, which is acceptable given the LUMO energy of commonly used OSC acceptors. Thus, the KL_{MeOH} -tunable WF of the binary CIL enables matching to a variety of acceptors used in OSCs.

2.2. Device Performance

The performance of the $BCP:KL_{MeOH}$ binary CILs is evaluated using the PM6:Y6 OSC system with the architecture of $ITO/PEDOT:PSS/PM6:Y6/BCP:KL_{MeOH}/Ag$. As depicted in **Figure 3**a, the energy barrier from Y6 to the cathode follows the change of the WF of the binary CILs, which means the KL_{MeOH} ratio from 0% to 50% is always matched for electron extraction at the cathode interface in Y6 based OSCs.

The current density versus voltage ($J-V$) curves of the binary CILs based OSCs are characterized as presented in Figure 3b, the statistics of PCE values (KL ratio 0% and 50%) are shown in Figure 3c, and the KL_{MeOH} ratio based V_{oc} and PCE curves and detailed photovoltaic parameters are summarized in Figure 3d and **Table 1**. The OSCs with $BCP:KL_{MeOH}$ binary CILs show highly interesting results where the champion device with 50% ratio of KL_{MeOH} yields a PCE of 15.73% with V_{oc}, J_{sc}, and fill factor (FF) of 0.855 V, 25.09 mA cm^{-2} and 73.3%, respectively. A distinctly enhanced PCE compared to neat BCP in $BCP:KL_{MeOH}$ based devices can be observed, possibly attributing to the sensitivity of Y6-like FREAs to BCP. To further understand the charge dynamic of the $BCP:KL_{MeOH}$ CILs based OSCs with different ratio of KL_{MeOH}, we measure the field (V_{eff}) dependence of photocurrent density (J_{ph}). The J_{ph} quickly saturates for $V_{eff} > 1$ V for all conditions (Figure S6b, Supporting Information). As shown in Figure 3e, we calculate the charge extraction probability $P(E,T)$ in the OSCs to evaluate the charge extraction properties of the blend films by normalizing J_{ph} with respect to the saturation current J_{sat} (J_{ph}/J_{sat}).[52] The obtained charge collection probability (η_{coll}) at the maximum power point (Mpp) as shown in the solid dots follows the OSC performance with the best value of 90.3% in 50% KL_{MeOH} ratio. The evolution of the η_{coll} indicates that the reduced charge collection either in BCP rich or KL_{MeOH} rich binary CILs affects the OSC performance. The enhancement of J_{sc} was also confirmed by the corresponding external quantum efficiency (EQE) measurements shown in Figure 3f. The device with binary CIL exhibits a stronger response than neat BCP as the interface layer in all the visible range, which in line with the increased photocurrent. The calculated J_{sc} with the values of 24.7 and 22.7 mA cm^{-2} were obtained by integrating the EQE, in consistent with the J_{sc} values measured from the solar simulator.

**ADVANCED
SCIENCE NEWS**

www.advancedsciencenews.com

**ADVANCED
MATERIALS**

www.advmat.de
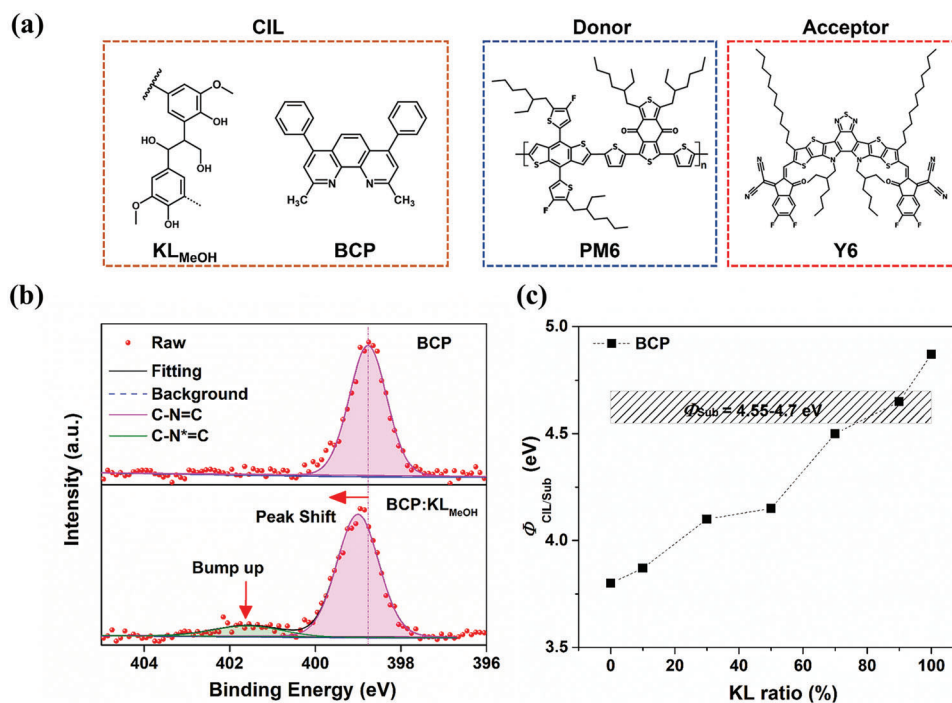
Figure 2. a) Molecular structures of binary cathode interface layer (CIL) materials. b) The XPS N1s core level spectra of binary CIL films. c) Summarized work function (WF) evaluation of binary CILs with different kraft lignin (KL) ratio.
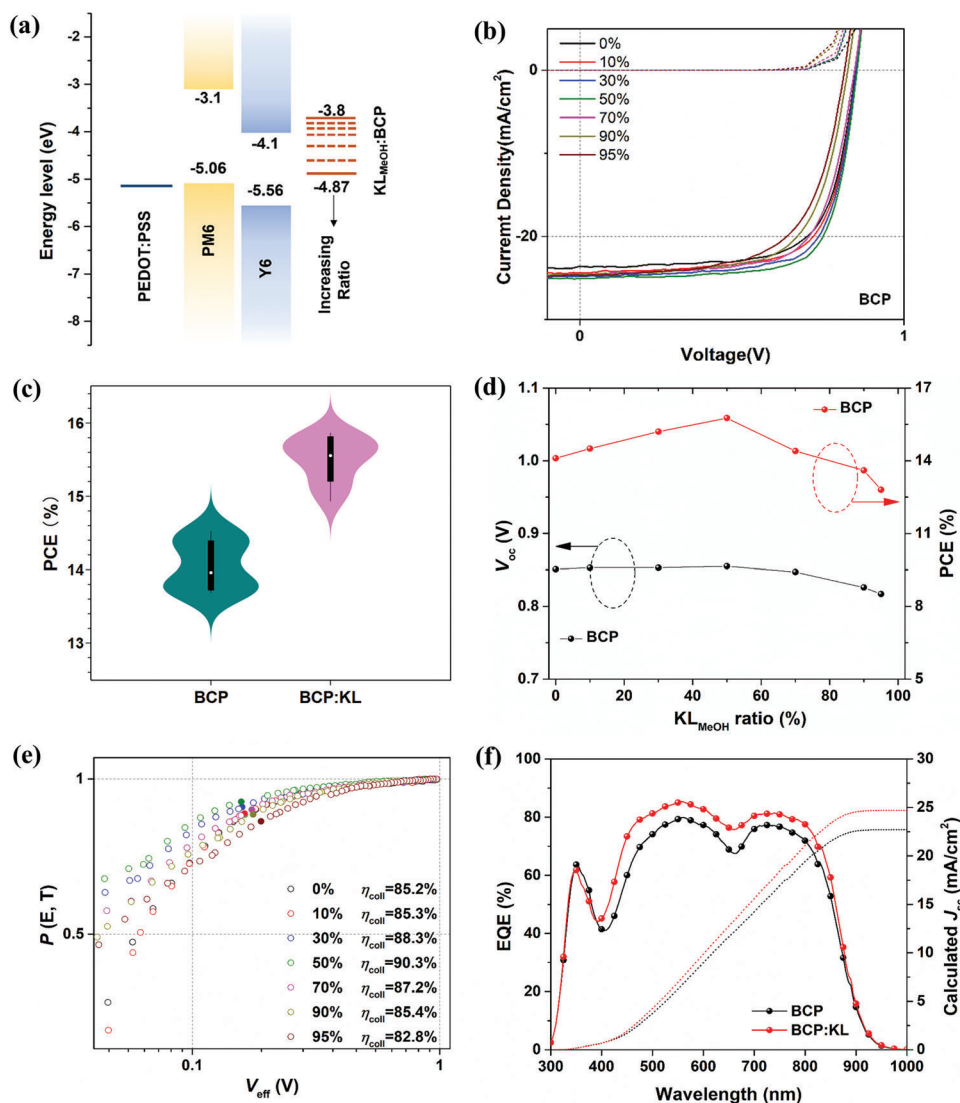
Figure 4a,b compares the photovoltaic parameters of devices employing $BCP:KL_{MeOH}$ or neat BCP CILs under dark condition over time. The devices were aged inside glovebox without any external factor (water, oxygen, and illumination) for up to 8 days. The device using the neat BCP CIL show an 80% loss of the initial efficiency when the device was stored in the N_2 atmosphere under dark in a week. This dramatic loss in PCE is due to the multifaceted degradation of V_{oc}, FF, and J_{sc}. However, the device using the $BCP:KL_{MeOH}$ CILs exhibited much better inherent stability with a PCE drop about 10% in a week. This result thus gives direct evidence that

the exacerbated interfacial problem over time between BCP and active layer can be effectively alleviated by the additional KL_{MeOH}.

The relations between J_{sc} or V_{oc} and light intensity (P_{light}) are further investigated to explore the charge recombination in the degraded devices.[53–55] As shown in Figure 4c, the calculated slope in the power-law dependence ($J_{sc} \propto P_{light}^{\alpha}$) is close to unity for all the conditions, which means weak biomolecular recombination for all. In addition, the ideality factor n is calculated from the slope of nkT/q in the function of $V_{oc} \propto nkT/q \ln P$ (k is Boltzmann constant, q is elementary charge, and T is temperature).

Table 1. Photovoltaic parameters of organic solar cells (OSCs) with bathocuproine (BCP) based cathode interface layers (CILs) with different KL_{MeOH} ratio.

Ratio (KL_{MeOH})	V_{oc} [V]	J_{sc} [mA cm^{-2}]	FF	PCE	J_{sc}^{Cal} [mA cm^{-2}] J_{sc}^{Cal}	WF [eV]
0%	0.851 (0.850 ± 0.02)	23.58 (23.53 ± 0.37)	70.0% (69.1% ± 0.9%)	14.11% (14.06% ± 0.36%)	22.7	3.80
10%	0.853 (0.853 ± 0.01)	24.41 (24.18 ± 0.28)	70.0% (69.7% ± 1.5%)	14.52% (14.44% ± 0.23%)	–	3.87
30%	0.853 (0.853 ± 0.01)	24.82 (24.63 ± 0.22)	71.9% (70.7% ± 0.8%)	15.24% (15.03% ± 0.29%)	–	4.06
50%	0.855 (0.856 ± 0.01)	25.09 (24.91 ± 0.21)	73.3% (72.5% ± 1.5%)	15.73% (15.42% ± 0.44%)	24.7	4.15
70%	0.847 (0.847 ± 0.01)	24.51 (24.43 ± 0.11)	69.2% (68.4% ± 0.8%)	14.42% (14.31% ± 0.16%)	–	4.5
90%	0.826 (0.826 ± 0.01)	24.61 (24.45 ± 0.17)	66.7% (65.3% ± 1.4%)	13.60% (13.41% ± 0.26%)	–	4.65
95%	0.817 (0.815 ± 0.02)	24.72 (24.56 ± 0.17)	63.4% (62.1% ± 1.3%)	12.78% (12.61% ± 0.21%)	–	–

ADVANCED
SCIENCE NEWS

www.advancedsciencenews.com

ADVANCED
MATERIALS

www.advmat.de

Figure 3. a) Energy levels of the functional layers. b) J–V curves of the organic solar cells (OSCs) with different KL_{MeOH} ratio. c) Violin plots of PCE distribution of OSCs with $BCP:KL_{MeOH}$ in ratio of 0% and 50%. d) KL_{MeOH} ratio versus V_{oc} and PCE of the OSCs. e) $P(E,T)$ versus voltage curves of OSCs with $BCP:KL_{MeOH}$ cathode interface layer (CIL). f) External quantum efficiency (EQE) spectra and integrated J_{sc} of OSCs with $BCP:KL_{MeOH}$ in ratio of 0% and 50%.

The ideality factor typically indicates the competition between trap-assisted recombination ($n = 2$) and biomolecular recombination ($n = 1$) in an ideal interface contact, as most OSC materials exhibit a distribution of trap states extending into the electronic band gap, which can be extracted by plotting V_{oc} versus the natural logarithm of P_{light} as shown in Figure 4d. However, the comparison of ideality factors shows an uncommon result that the relatively poor device with BCP CIL shows a smaller n_{id} than the $BCP:KL_{MeOH}$ based device, in the values of 1.01 and 1.07 at moderate intensities (close to 1 sun) respectively. Whereas the n_{id} of neat BCP CIL based device continuously decrease to 0.92 in 1 day under degradation. To explain this, we emphasize the possibility of surface recombination in the devices. Surface recombination typically is proportional to the excess minority carrier concentration at the contact, as a result, n_{id} decreases with in-

creasing mobility and approaches 1 at high mobilities if we consider diffusion-limited surface recombination with Ohmic contacts alone in OSCs.[56] However, if bulk recombination limits the transport within the active layer, the additional n_{id} reduction will be caused by a non-Ohmic contact. The appearance of $n_{id} < 1$ was theoretically confirmed in the device simulation and obtained for unoptimized energy levels at the TiO_2-$P3HT:PC_{60}BM$ interface.[57,58] In our case, we assume that the device based on neat BCP suffers from more surface recombination, possibly caused by energy level mismatched interfaces and/or traps in the interface region. In addition, the mismatch at the photoactive layer (PAL)/BCP CIL interfaces will significantly increase due to the fast degradation of neat BCP CIL OSCs. Similar surface recombination could also occur in the binary CIL based devices; however, it can be effectively suppressed by the

2307646 (5 of 12)
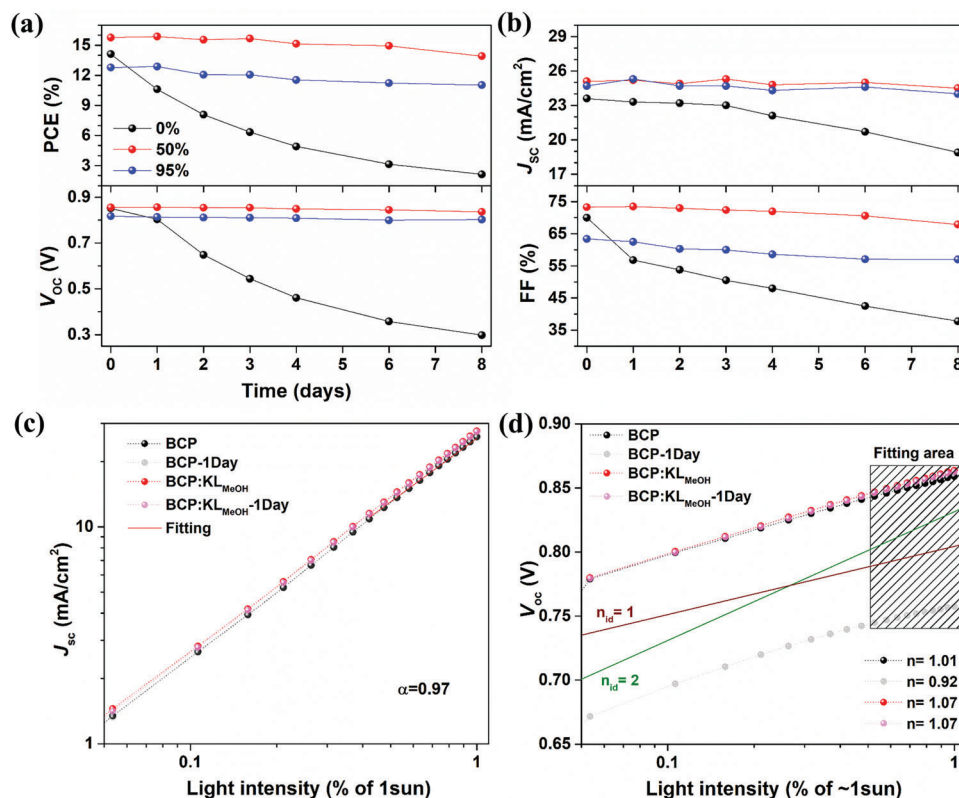
Figure 4. a,b) Photovoltaic parameters degradation of organic solar cells (OSCs) with BCP:KL$_{MeOH}$ cathode interface layer (CIL). Light intensity-dependent c) J_{sc} and d) V_{oc} of OSCs with pure bathocuproine (BCP) and BCP:KL$_{MeOH}$ in ratio of 50% with or without 1 day degradation.

residual KL$_{MeOH}$ at the cathode interface. The abovementioned results thus confirm that the binary CIL strategy can successfully solve the problem of the undesirable interaction between Y6 based active layer and the BCP CIL, resulting in enhanced OSC performance and stability.

2.3. Device Simulations

To gain the deeper understanding of the device degradation, we conducted numerical device simulations by a drift–diffusion model.[59,60] The simplistic metal–insulator–metal model with the PAL considered an effective semiconductor sandwiched between two metal contacts is adopted. The key parameters of the PM6:Y6 blend, such as the charge carrier mobilities and the recombination rate in the bulk, were taken from literature [61–63] and optimized in narrow range until a good fit with the experiment was reached. While the anode was considered ideal, the properties of the cathode (mimicking the PAL/CIL interface) were varied. As shown in Figure S7a (Supporting Information), the model gives an excellent description of the measured J–V curve of an unaged device with neat BCP, which is used as a baseline.

We attempted to model the degradation by introducing an injection barrier at the cathode (see Figure S7b, Supporting Information, for the simulated J–V curves). An injection barrier, i.e., an energetic offset between the work function of the contact and the respective transport level in the PAL, strongly effects the density of minority carriers in the vicinity of the contact an gives rise to surface recombination.[64,65] **Figure 5**a shows that varying the cathode injection barrier from 0 eV (ideal contact) to 0.7 eV leads to a significant degradation of both V_{oc} and FF that is consistent with the degradation seen in experiment (Figure 4a,b). Hence, the rapid degradation of the devices with neat BCP can effectively be described by an increasing energetic mismatch at the PAL/BCP interface over time. The injection barrier is directly proportional to the build-in voltage, which in case of a nonideal contact limits V_{oc} through surface recombination, as discussed by Sandberg et al.[66] To further verify our hypothesis, we modeled the light intensity dependence of V_{oc}, which is shown in Figure 5b. Cleary, for devices with a significant injection barrier at the cathode, the slope of V_{oc} plotted versus the logarithm of the light intensity shows a transition from kT/q to values lower than kT/q (equivalent to a change of the ideality factor from $n_{id} = 1$ to $n_{id} < 1$) at mid to high light intensity. This is due to surface recombination becoming increasingly important over bulk recombination.[8] The simulations are consistent with the experimental observation in the aged BCP device (Figure 4d), further conforming that the degradation is mainly caused by surface recombination at the PAL/BCP interface. For the BCP:KL$_{MeOH}$ devices, however, the degradation is largely absent, which suggests that the main effect of KL$_{MeOH}$ is to prevent the energetic structure at the interface from changing. Possible stabilization mechanisms will be discussed in the following section.

2.4. Degradation Mechanism

To clarify the origin of the poor performance and stability in BCP CIL based OSCs compared with the BCP:KL$_{MeOH}$ CIL, we monitor the morphology evolution on aged CILs on the surface of PALs with the structures of glass/PM6:Y6/BCP and glass/PM6:Y6/BCP:KL$_{MeOH}$ (The ratio of KL$_{MeOH}$ is 50% in these degradation experiments) by AFM. As shown in **Figure 6**a, solution-processed BCP films exhibit clear aggregation features on the PM6:Y6 surface with an R_q of 3.21 nm, possibly attributed to mismatched surface energy. However, after 7 days storage in the same condition as a device, the BCP film show much smoother surface with the R_q of 0.8 nm, depicting no aggregation feature at all. We propose that this is due to chemical interaction and even diffusion of BCP into the PAL. In contrast for the BCP:KL$_{MeOH}$ binary CIL case, the aggregation features are diluted by the KL$_{MeOH}$ components and there is only a slightly reduction of R_q after 7 days storage.

Given the obvious interactions involving BCP at the PAL interface, we carried out UV–Vis absorption of the aged films based on neat BCP or binary BCP:KL$_{MeOH}$, as tracking the change of the absorption peaks for the donor and acceptor can help to further clarify the relationship between device degradation and optoelectronic materials properties. As shown in Figure 6b, the main peak of PM6 at 630 nm is consistent in all the conditions, whereas the absorption of the Y6 peak at ≈730 nm for the BCP based bilayer film clearly decreases compared to the BCP:KL$_{MeOH}$ based bilayer film. After 7 days degradation, the BCP based bilayer film exhibits a further reduction and a minor blue-shift of Y6 absorption as shown in the figure insert. The change of the Y6 absorption peak in this long-wavelength spectral region suggests the loss of intramolecular charge transfer in the chemical structure from the donor moiety to the acceptor moiety, which refers to the breaking of conjugated bridge C = C bonds. Thus, the optical and electrical properties of Y6 are significantly changed and degraded by the reaction with BCP, However, almost no degradation of the Y6 absorption could be observed in the BCP:KL$_{MeOH}$ based film in 7 days. This result is in accordance with the change in OSC-device ideality factors, which clarifies the effect of the additional KL$_{MeOH}$ in enhancing device stability.

The elemental bond variations are shown by the XPS N1s analysis in Figure 6c, suggesting a significant change in Y6 and BCP distribution at the top surface in the depth of ≈10 nm. We deconvolute the Y6 N1s spectrum with two main components at 399.2 and 400.6 eV, respectively, and a satellite feature at 402.7 eV. Based on the chemical structure of the Y6 molecule, the filled pink peaks are assigned to cyano groups (C ≡ N), and the other filled green peaks with slightly broader FWHM but similar spectral weight are assigned to C-N and N-S bonds. Then the N1s peak for BCP can be fitted (filled purple peaks) with a slight shift from 398.55 to 398.70 eV for neat BCP to BCP:KL$_{MeOH}$. A huge reduction of the purple peak intensity of about two thirds is observed in the neat BCP after 7 days storage, whereas similar but significantly less reduction is obtained in the BCP:KL$_{MeOH}$ case. Note that the N bonds of Y6 are not strongly affected by the BCP, instead BCP reacts as a nucleophile with the Y6 C = C linkage. This result is consistent with our observation in AFM images, indicating that the KL$_{MeOH}$ partially prevents BCP diffusion into and reaction with Y6 in the PAL. To gain insight into possible potential steps at the CIL/PAL interface, UPS measurements of the films were applied. Only minor WF shifts of 0.05 eV were obtained in both cases, as shown in Figure S8 (Supporting Information). Since UPS is an extremely surface sensitive measurement, we do not see the BCP at the buried interface with the PAL, and hence not the trap density of states and/or energetic mismatch induced by the BCP-FREA interaction.

2.5. Application in Other Solar Cells

We further adopt the binary CIL BCP:KL$_{MeOH}$ in higher performance OSCs with ternary active layers based on donor, PC$_{60}$BM/PC$_{70}$BM and other FREA NFAs. The molecular structures of these OSC materials are presented in Figure S9 (Supporting Information). It is noted that the usage of the fullerene can further improve the stability of FREA in NFA-OSCs, owing to charge transfer from BCP to fullerene which reduces the electron density of the lone electron pairs at the N atoms.[51,67] The time-dependent photovoltaic parameters are plotted in **Figure 7**, in which the devices were stored in the same condition as binary devices (detailed J–V curves see Figure S10, Supporting Information). The PM6:Y6:PC$_{70}$BM ternary devices using either
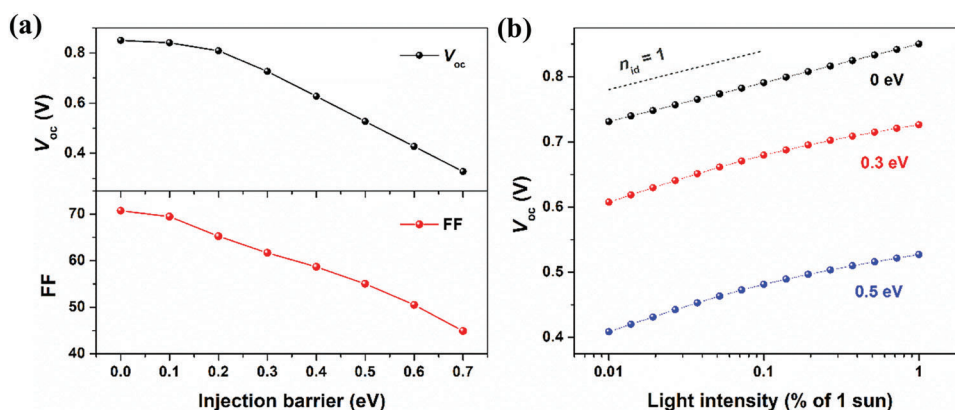
Figure 5. Numerical device simulations of PM6:Y6 solar cells using a drift–diffusion model. a) V_{oc} and fill factor (FF) modeled for different injection barriers at the cathode, while the anode was considered ideal. b) Light-intensity dependence of V_{oc} for a barrier height of 0, 0.3, and 0.5 eV, respectively.
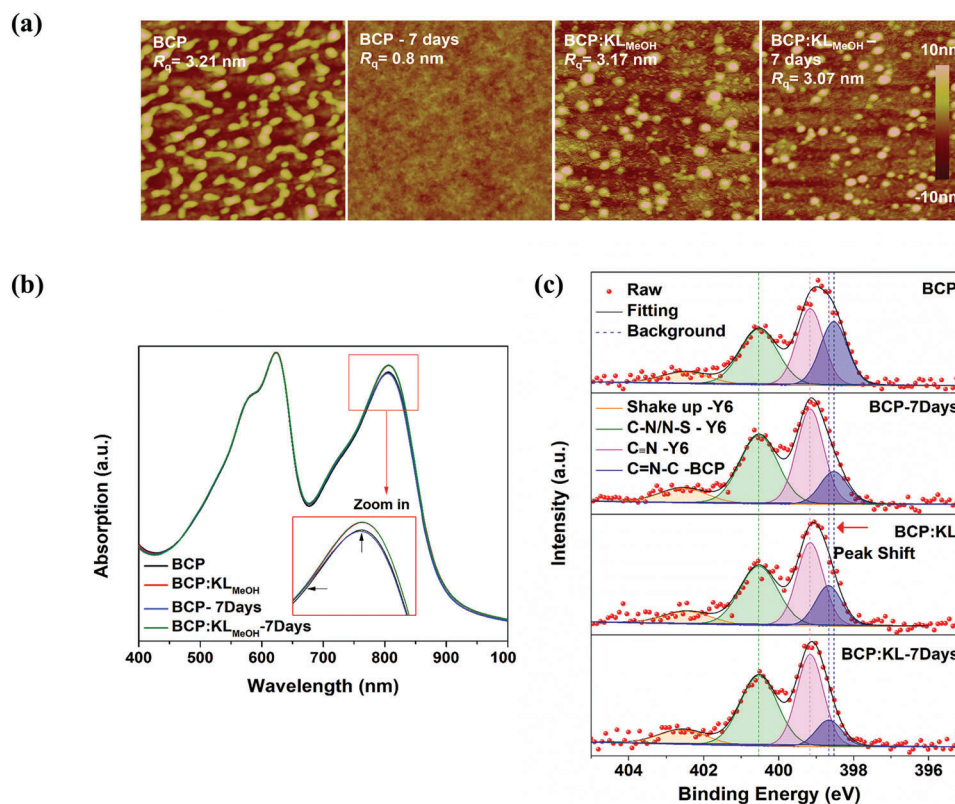
Figure 6. a) Atomic force microscopy (AFM) images (2 × 2 µm), b) UV–Vis absorption, and c) XPS N1s core level spectra of bilayer films based on neat bathocuproine (BCP) and BCP:KL$_{MeOH}$ with and without 7 days degradation.

neat BCP and BCP:KL$_{MeOH}$ (The ratio of KL$_{MeOH}$ is 50%) as CILs have the PCE of 16.8%, with the same photovoltaic parameters at the beginning. However, the binary CIL based devices show better stability compared to the neat BCP ones in the 1 month degradation test. In addition, the ternary devices with neat BCP CIL exhibit much better stability compared to the devices without PC$_{70}$BM, which is in line with our expectations. The OSCs with the ternary active layer PM6:BTP-ec9:PC$_{70}$BM have a similar stability enhancement by using the BCP:KL$_{MeOH}$ CIL. Espe-

cially, when D18-Cl:N3:PC$_{60}$BM is adopted, a superior PCE of 18.4% can be achieved by using the BCP:KL$_{MeOH}$ CIL in the devices, and device stability is much enhanced compared to the corresponding neat BCP CIL devices. All ternary devices are significantly less stable with just the neat BCP CIL where especially D18-Cl:N3:PC$_{60}$BM degrades in just 3 days even with the help of PC$_{60}$BM.

The BCP:KL$_{MeOH}$ CIL can be also used in the perovskite solar cells (PSCs), even though the performance enhancement may be
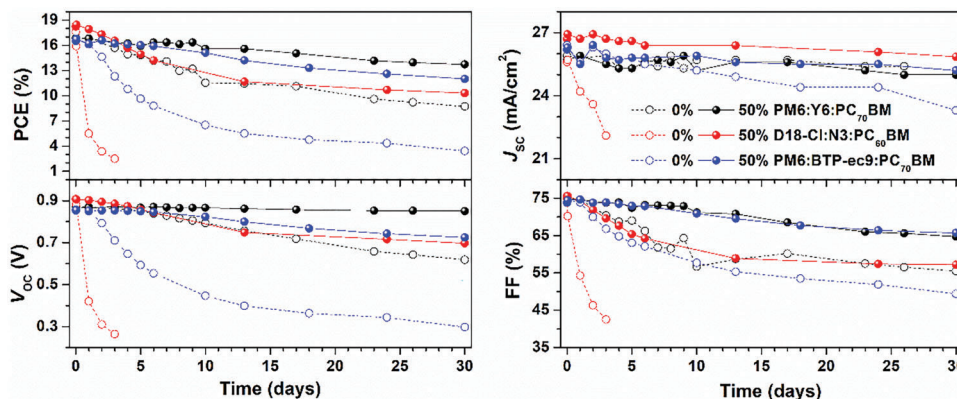
Figure 7. Photovoltaic parameters degradation of ternary organic solar cells (OSCs) with bathocuproine (BCP) and BCP:KL$_{MeOH}$. The color of the curves means the OSC system that PM6:Y6:PC$_{70}$BM (black), D18-Cl:N3:PC$_{60}$BM (red), and PM6:BTP-ec9:PC$_{70}$BM (blue). The open dot and solid dot in the curves mean the kraft lignin (KL) ratio is 0% and 50%, respectively.
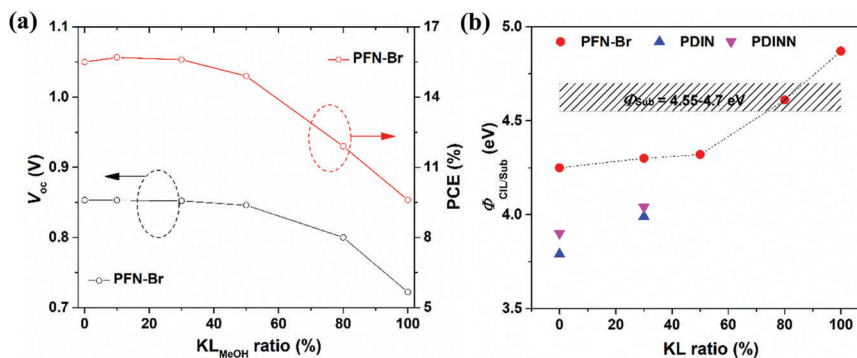
Figure 8. a) KL_{MeOH} ratio versus V_{oc} and PCE of the organic solar cells (OSCs) with PFN-Br:KL_{MeOH} cathode interface layers (CILs). b) Summarized work function (WF) evaluation of binary CILs.

limited, the use of the KL-based CIL demonstrates excellent compatibility (see Figure S11 and Table S2, Supporting Information).

2.6. Viability of KL in Other Binary CILs

We finally investigated the viability of the KL in other binary CILs by using other CIL materials such as N,N"-Bis[3-(dimethylamino)propyl]perylene-3,4,9,10-tetracarboxylic diimide (PDIN), *N,N"*-bis{3-[3-(dimethylamino)propylamino]propyl}perylene-3,4,9,10-tetracarboxylic diimide (PDINN) and Poly(9,9-bis(3'-(*N,N*-dimethyl)-*N*-ethylammoinium-propyl-2,7-fluorene)-alt-2,7-(9,9-dioctylfluorene))dibromide (PFN-Br). The molecular structures of these CIL materials are shown in Figure S12 (Supporting Information). Among these CIL materials, PFN-Br shows excellent compatibility to KL_{MeOH} similar to BCP (see Figure S13, Supporting Information, the morphology evolution of PFN-Br:KL_{MeOH} films depending on KL_{MeOH} ratio). The PFN-Br:KL_{MeOH} binary CILs work well in the PM6:Y6 OSC system, as shown in **Figure 8**a, we summarized the obvious change of the photovoltaic parameters in the KL_{MeOH} ratio based V_{oc} and PCE curves, and the detailed *J–V* curves and photovoltaic parameters are presented in Figure S14 and Table S1 (Supporting Information). As demonstrated, the PM6:Y6 systems with neat PFN-Br exhibited a typical PCE of 15.54% with open circuit voltage (V_{oc}), short circuit current density (J_{sc}), and fill factor (FF) of 0.85 V, 25.87 mA cm^{-2}, and 70.4%, respectively. When the KL_{MeOH} ratio increases to 30%, there is almost no change in the PCE with other photovoltaic parameters. A continued increase of KL_{MeOH} ratio to above 30% in the PFN-Br:KL_{MeOH} binary CILs lead to the beginning of the PCE drop, attributed to increasing KL_{MeOH} caused energetic mismatch at more and more regions of the cathode interface. The OSC performance evolution is consistent with the UPS results of the binary CIL, as shown in Figure 8b (Figure S15a, Supporting Information), the summarized ratio-dependent WF. The WF of the PFN-Br based binary films also can be tuned in the range of 4.25 to 4.85 eV, but unlike BCP, the WF slowly changes between 0% to 50% KL_{MeOH} content and then a fast change rate from 50% to 100%. Since there is no shift obtained in the XPS N1s spectra for the PFN-Br based binary films, which we attribute to that the cationic N (C_4N^+) of PFN-Br, refer to main peak 403.1 eV, cannot donate significant electron density to KL_{MeOH} (see

Figure S16, Supporting Information). Herein, we proposed that the WF change is more affected by the phased separation of KL_{MeOH} and PFN-Br.

The binary CILs based on PDIN and PDINN did not work as well in the OSCs. We manage to obtain tunable WF by blending with KL, but too strong interaction between PDIN/PDINN to KL induced significant aggregation problems in the films even at low KL ratios (see Figures S13, S15b, and S17, Supporting Information, for details). This illustrates that for some CIL materials the interaction with KL must be modified by a third component in order to achieve suitable morphologies.

3. Conclusion

In summary, we demonstrated the utility of binary CIL strategy based on the industrial solvent fractionated LignoBoost KL in highly efficient OSCs. Introducing large ratios of KL into the binary CILs can successfully enhance sustainability of the CIL materials. In particular, BCP:KL_{MeOH} binary CILs significantly improve the stability of both binary and ternary PAL OSC devices compared to the corresponding neat BCP CIL based devices, and the PCE is also increased. The mechanism underlying the improvement of OSCs has been investigated from both materials and device characterizations, which mainly ascribed to KL_{MeOH} blocking diffusion and reaction between BCP and NFAs. Our results demonstrate that the binary CIL strategy based on industrial KL is a simple and effective way to improve the performance of OSCs, and more importantly, to reawaken low-cost, intrinsically stable classic interface materials from the OLED technology by pairing them with the recently emerging FREA NFAs.

4. Experimental Section

Materials: KF used in this work was received from prof. Mats Johansson. PM6, D18-Cl, Y6, N3, and BTP-ec9 were purchased from Solarmer Materials Inc. PFN-Br, PC$_{60}$BM, and PC$_{70}$BM were purchased from 1-material (Canada). PEDOT:PSS (Clevios P VP AI 4083) was purchased from Heraeus Materials. The other materials and solvents were commercially available. All the materials were used as received.

OSC Fabrication and Characterizations: The configuration of ITO/PEDOT:PSS/active layer/CIL/Ag was used to fabricate the organic solar cell devices. The precleaned ITO substrates were routinely cleaned through sonication in detergent, followed by sequential washing

ADVANCED
SCIENCE NEWS

www.advancedsciencenews.com

**ADVANCED
MATERIALS**

www.advmat.de

in deionized water, acetone, and 2-propanol. After drying by nitrogen blowing, ITO substrates were treated by UV-ozone for 20 min. The anode buffer layer PEDOT:PSS was spin-coated at 4000 rpm onto ITO-coated glass substrates, followed by annealing at 120 °C for 20 min to remove the water. Then the substrates were transferred into the N_2-filled glove box for preparing the photoactive layer. The PM6:Y6 mixed solution was made with a concentration of 16 mg mL^{-1} and a mass ratio of 1:1.2 in chloroform, the solution of PM6:Y6:PC$_{70}$BM ternary blend was prepared by dissolving with a concentration of 15.4 mg mL^{-1} and a mass ratio of 1:1:0.2 in chloroform, the solution of D18-Cl:N3:PC$_{60}$BM ternary blend was prepared by dissolving with a concentration of 15 mg mL^{-1} and a mass ratio of 1:1.4:0.1 in chloroform, the solution of PM6:BTP-ec9:PC$_{70}$BM ternary blend was prepared by dissolving with a concentration of 17 mg mL^{-1}, and a mass ratio of 1:1:0.2 in chlorobenzene, all the solutions were stirred for all night under 50 °C. Before the fabrication of the active layer, 0.5% chloronaphthalene (CN) and 3% DIO by volume as additive were added into chloroform and chlorobenzene solutions respectively, then stirred for half an hour. All the solutions were directly spin-coated on PEDOT:PSS to achieve about 100 nm thickness. After that, the PM6:Y6 active layer was annealed at 85 °C for 10 min, PM6:BTP-ec9:PC$_{70}$BM and PM6:Y6:PC$_{70}$BM active layers were annealed at 100 °C for 10 min. The reference CIL solution was prepared by dissolving BCP, PFN-Br, PDIN, and PDINN in methanol (0.3% volume ratio of acetic acid for PDIN) with the concentration of 0.5, 0.5, 1, and 1 mg mL^{-1}, respectively. To prepare the binary CIL, KL$_{MeOH}$ was mixed with BCP, PFN-Br, PDIN, and PDINN in mentioned weight ratio in methanol, the concentration of the binary solution was kept same to the single component solution. The CIL was fabricated by spin-coating on the top of the active layer. Finally, the coated substrates were directly transferred to a vacuum deposition system mounted inside of the glove box. The cathode Ag (100 nm) was thermally evaporated via a shadow mask under vacuum at 3×10^{-7} mbar. The effective device area was 0.043 cm^2. J–V characteristics were recorded by a Paios platform under illumination of an AM1.5 solar simulator with an intensity of 100 mW cm^{-2} in the glovebox. The light intensity was determined by a standard silicon photodiode. As for the light intensity-dependent measurements, the light source was a white LED which was integrated with the Paios platform. EQE profiles were measured by a Newport Merlin lock-in amplifier. A calibrated silicon detector (PRL-12, Newport, USA) with known photoresponse was utilized as a reference.

PSC Fabrication and Characterizations: The configuration of ITO/Meo-2PACZ/CsFAMA/PCBM/CIL/Ag was used to fabricate the organic solar cell devices. The ITO substrates were cleaned as mentioned in OSC fabrication and treated with UV–ozone for 15 min. The Meo-2PACz solution with the concentration of 0.5 mg mL^{-1} in ethanol was spin-coated on the ITO substrates at 5000 rpm for 30 s, and then annealed at 100 °C for 10 min in glovebox. The triple cation perovskite precursor solution was consisted of "FAMA" solution, which was prepared by mixing 1.4 M FAPbI3 and MAPbBr3 perovskite precursor in DMF:DMSO (4:1 volume ratio, v:v) with 9% PbX2 excess respectively (X = I or Br) in a volume ratio of 95:5, 4% volume ratio of CsI solution in DMSO, and 15 mol% MACl. To deposit the perovskite films, 70 µL of the precursor was spin-coated on the substrates at 4000 rpm for 40 s, then 200 µL antisolvent chlorobenzene was slowly dripped onto the center of the film during the spinning, and finally annealing at 100 °C for 60 min. After the perovskite deposition, PCBM with 20 mg mL^{-1} in CB was deposited on the perovskite layer at 1800 rpm for 40 s, and then the CILs with 0.5 mg mL^{-1} in methanol was spin coated at 4000 rpm for 30 s. Finally, the 100 nm Ag electrode was thermally deposited by evaporation. The effective device area was 0.05 cm^2. J–V characteristics were recorded by a Keithley 2400 system under illumination of an AM1.5 solar simulator with an intensity of 100 mW cm^{-2} in the glovebox.

Photoelectron spectroscopy: The PES samples were spin-coated in glovebox on ITO substrates, then directly and quickly transferred into the load lock chamber of the ultrahigh vacuum (UHV) system for the following steps. The UPS experiments were done in a home-designed spectrometer, the excitation source was monochromatic He I radiation with photon energy of 21.22 eV. The work function was derived from the secondary electron cut-off and the vertical IP from the frontier edge of the occupied den-

sity of states with an error margin of ±0.05 eV. XPS was performed with a Scienta-200 hemispherical analyzer using monochromatized Al Kα source with photon energy of 1486.6 eV. All photoelectron spectroscopy measurements were carried out with a base pressure lower than 1×10^{-9} mbar.

NEXAFS Measurement: NEXAFS Measurements were performed at the FlexPES (Flexible Photoelectron Spectroscopy) beamline at MAX IV synchrotron radiation facility in Lund, Sweden, with horizontally linear polarized light in the energy range of 40–1500 eV. The defocused beam spot size at sample was ≈2×1 mm to minimize any possible radiation damage. Angle-resolved NEXAFS spectra were collected in both partial electron yield (PEY) and total electron yield (TEY) detection modes with multichannel plate and sample drain current, respectively. The collected spectra were normalized to the incident photon flux. The linear pre-edge background was then subtracted, and the resulting spectra were normalized to the post-edge intensity in the continuum region.

AFM Measurement: AFM measurements were performed with a dimension 3100 system using antimony-doped silicon cantilevers in tapping mode.

UV–Vis Measurement: UV–Vis absorption spectra were measured with a Perkin Elmer Lambda 900 UV–Vis–NIR absorption spectrometer.

Device Simulations: Numerical simulations of PM6:Y6 devices were performed using a one-dimensional drift–diffusion model. The active bulk heterojunction layer was modeled as an effective semiconductor sandwiched between two metal contacts. The contacts were characterized by their surface recombination velocity and work function, the latter defining an injection barrier at the active layer/metal interface. Here, the anode was considered ideal (negligible surface recombination, injection barrier = 0 eV), while for the cathode, a finite surface recombination velocity was assumed, and the injection barrier was varied. Recombination in the bulk was assumed to be purely bimolecular with a rate equation $R = k_2 np$, where n and p is the density of electrons and holes, respectively, and k_2 the recombination rate constant. The key input parameters were optimized in a narrow range to compensate for the variations in preparation conditions between laboratories.

Supporting Information

Supporting Information is available from the Wiley Online Library or from the author.

Acknowledgements

Conflict of Interest

The authors declare no conflict of interest.

Data Availability Statement

The data that support the findings of this study are available from the corresponding author upon reasonable request.

Keywords

[1] O. Inganäs, *Adv. Mater.* **2018**, *30*, 1800388.

[2] Y. Jiang, X. Dong, L. Sun, T. Liu, F. Qin, C. Xie, P. Jiang, L. u. Hu, X. Lu, X. Zhou, W. Meng, N. Li, C. J. Brabec, Y. Zhou, *Nat. Energy* **2022**, *7*, 352.

[3] S. Liu, J. Yuan, W. Deng, M. Luo, Y. Xie, Q. Liang, Y. Zou, Z. He, H. Wu, Y. Cao, *Nat. Photonics* **2020**, *14*, 300.

[4] L. Meng, Y. Zhang, X. Wan, C. Li, X. Zhang, Y. Wang, X. Ke, Z. Xiao, L. Ding, R. Xia, H.-L. Yip, Y. Cao, Y. Chen, *Science* **2018**, *361*, 1094.

[5] C. Yan, S. Barlow, Z. Wang, H. Yan, A. K.-Y. Jen, S. R. Marder, X. Zhan, *Nat. Rev. Mater.* **2018**, *3*, 18003.

[6] Y. Cui, Y. Xu, H. Yao, P. Bi, L. Hong, J. Zhang, Y. Zu, T. Zhang, J. Qin, J. Ren, *Adv. Mater.* **2021**, *33*, 2102420.

[7] L. Zhu, M. Zhang, J. Xu, C. Li, J. Yan, G. Zhou, W. Zhong, T. Hao, J. Song, X. Xue, Z. Zhou, R. Zeng, H. Zhu, C.-C. Chen, R. C. I. Mackenzie, Y. Zou, J. Nelson, Y. Zhang, Y. Sun, F. Liu, *Nat. Mater.* **2022**, *21*, 656.

[8] A. J. Gillett, A. Privitera, R. Dilmurat, A. Karki, D. Qian, A. Pershin, G. Londi, W. K. Myers, J. Lee, J. Yuan, S.-J. Ko, M. K. Riede, F. Gao, G. C. Bazan, A. Rao, T.-Q. Nguyen, D. Beljonne, R. H. Friend, *Nature* **2021**, *597*, 666.

[9] J. Hou, O. Inganäs, R. H. Friend, F. Gao, *Nat. Mater.* **2018**, *17*, 119.

[10] M. Fahlman, S. Fabiano, V. Gueskine, D. Simon, M. Berggren, X. Crispin, *Nat. Rev. Mater.* **2019**, *4*, 627.

[11] J.-K. Tan, R.-Q. Png, C. Zhao, P. K. Ho, *Nat. Commun.* **2018**, *9*, 3269

[12] D. Li, M. H. Nielsen, J. R. I. Lee, C. Frandsen, J. F. Banfield, J. J. De Yoreo, *Science* **2012**, *336*, 1014.

[13] Z. Tang, W. Tress, Q. Bao, M. J. Jafari, J. Bergqvist, T. Ederth, M. R. Andersson, O. Inganäs, *Adv. Energy Mater.* **2014**, *4*, 1400643.

[14] J. Yao, B. Qiu, Z.-G. Zhang, L. Xue, R. Wang, C. Zhang, S. Chen, Q. Zhou, C. Sun, C. Yang, M. Xiao, L. Meng, Y. Li, *Nat. Commun.* **2020**, *11*, 2726

[15] C. Feng, X. Wang, Z. He, Y. Cao, *Sol. RRL* **2021**, *5*, 2000753.

[16] Q. Zhang, C. Wang, X. Liu, M. Fahlman, *Sol. RRL* **2021**, *5*, 2000575.

[17] J. Yuan, Y. Zhang, L. Zhou, G. Zhang, H.-L. Yip, T.-K. i. Lau, X. Lu, C. Zhu, H. Peng, P. A. Johnson, M. Leclerc, Y. Cao, J. Ulanski, Y. Li, Y. Zou, *Joule* **2019**, *3*, 1140.

[18] X. Li, Q. Zhang, J. Yu, Y. Xu, R. Zhang, C. Wang, H. Zhang, S. Fabiano, X. Liu, J. Hou, *Nat. Commun.* **2022**, *13*, 2046.

[19] J. Bertrandie, J. Han, C. S. De Castro, E. Yengel, J. Gorenflot, T. Anthopoulos, F. Laquai, A. Sharma, D. Baran, *Adv. Mater.* **2022**, *34*, 2202575.

[20] S. Xiong, L. Hu, L. u. Hu, L. Sun, F. Qin, X. Liu, M. Fahlman, Y. Zhou, *Adv. Mater.* **2019**, *31*, 1806616.

[21] X. Zhu, L. Hu, W. Wang, X. Jiang, L. Hu, Y. Zhou, *ACS Appl. Energy Mater.* **2019**, *2*, 7602.

[22] Q. Kang, Q. i. Wang, C. An, C. He, B. Xu, J. Hou, *J. Energy Chem.* **2020**, *43*, 40.

[23] Q. Kang, L. Ye, B. Xu, C. An, S. J. Stuard, S. Zhang, H. Yao, H. Ade, J. Hou, *Joule* **2019**, *3*, 227.

[24] Z. Wu, C. Sun, S. Dong, X.-F. Jiang, S. Wu, H. Wu, H.-L. Yip, F. Huang, Y. Cao, *J. Am. Chem. Soc.* **2016**, *138*, 2004.

[25] Z.-G. Zhang, B. Qi, Z. Jin, D. Chi, Z. Qi, Y. Li, J. Wang, *Energy Environ. Sci.* **2014**, *7*, 1966.

[26] Q. Yin, K. Zhang, L. Zhang, J. Jia, X. Zhang, S. Pang, Q.-H. Xu, C. Duan, F. Huang, Y. Cao, *J. Mater. Chem. A* **2019**, *7*, 12426.

[27] H. Song, D. Hu, J. Lv, S. Lu, C. Haiyan, Z. Kan, *Adv. Sci.* **2022**, *9*, 2105575.

[28] S. Xiong, T. Hao, Y. Sun, J. Yang, R. Ma, J. Wang, S. Gong, X. Liu, L. Ding, M. Fahlman, Q. Bao, *J. Energy Chem.* **2021**, *55*, 265.

[29] S. Xiong, Z. Hou, S. Zou, X. Lu, J. Yang, T. Hao, Z. Zhou, J. Xu, Y. Zeng, W. Xiao, W. Dong, D. Li, X. Wang, Z. Hu, L. Sun, Y. Wu, X. Liu, L. Ding, Z. Sun, M. Fahlman, Q. Bao, *Joule* **2021**, *5*, 467.

[30] J. Yang, S. Xiong, T. Qu, Y. Zhang, X. He, X. Guo, Q. Zhao, S. Braun, J. Chen, J. Xu, Y. Li, X. Liu, C. Duan, J. Tang, M. Fahlman, Q. Bao, *ACS Appl. Mater. Interfaces* **2019**, *11*, 13491.

[31] Q. Zhang, H. Zhang, Z. Wu, C. Wang, R. Zhang, C. Yang, F. Gao, S. Fabiano, H. Y. Woo, M. Ek, *Sol. RRL* **2022**, *6*, 2200381.

[32] K. Alfonsi, J. Colberg, P. J. Dunn, T. Fevig, S. Jennings, T. A. Johnson, H. P. Kleine, C. Knight, M. A. Nagy, D. A. Perry, M. Stefaniak, *Green Chem.* **2008**, *10*, 31.

[33] C. Crestini, H. Lange, M. Sette, D. S. Argyropoulos, *Green Chem.* **2017**, *19*, 4104.

[34] M. Jawerth, M. Johansson, S. Lundmark, C. Gioia, M. Lawoko, *ACS Sustainable Chem. Eng.* **2017**, *5*, 10918.

[35] M. E. Jawerth, C. J. Brett, C. d. Terrier, P. T. Larsson, M. Lawoko, S. V. Roth, S. Lundmark, M. Johansson, *ACS Appl. Polym. Mater.* **2020**, *2*, 668.

[36] Y. Li, N. Hong, *J. Mater. Chem. A* **2015**, *3*, 21537.

[37] N. Hong, J. Xiao, Y. Li, Y. Li, Y. Wu, W. Yu, X. Qiu, R. Chen, H.-L. Yip, W. Huang, Y. Cao, *J. Mater. Chem. C* **2016**, *4*, 5297.

[38] Y. Wu, J. Wang, X. Qiu, R. Yang, H. Lou, X. Bao, Y. Li, *ACS Appl. Mater. Interfaces* **2016**, *8*, 12377.

[39] Y. Li, T. Liu, X. Qiu, Y. Zhou, Y. Li, *ACS Sustainable Chem. Eng.* **2018**, *7*, 961.

[40] H.-C. Hu, H. Xu, J. Wu, L. Li, F. Yue, L. Huang, L. Chen, X. Zhang, X. Ouyang, *Adv. Funct. Mater.* **2020**, *30*, 2001494.

[41] W. Boerjan, J. Ralph, M. Baucher, *Annu. Rev. Plant Biol.* **2003**, *54*, 519.

[42] F. S. Chakar, A. J. Ragauskas, *Ind. Crops Prod.* **2004**, *20*, 131.

[43] A. Duval, F. Vilaplana, C. Crestini, M. Lawoko, *Holzforschung* **2016**, *70*, 11.

[44] A.-S. JaaSkeläinen, T. Liitiä, A. Mikkelson, T. Tamminen, *Ind. Crops Prod.* **2017**, *103*, 51.

[45] Z. Y. Xie, L. S. Hung, S. T. Lee, *Appl. Phys. Lett.* **2001**, *79*, 1048.

[46] Y. Kijima, N. Asai, S.-I. Tamura, *Jpn. J. Appl. Phys.* **1999**, *38*, 5274.

[47] Y. Lin, B. o. Chen, F. Zhao, X. Zheng, Y. Deng, Y. Shao, Y. Fang, Y. Bai, C. Wang, J. Huang, *Adv. Mater.* **2017**, *29*, 1700607.

[48] R. Chen, B. Long, S. Wang, Y. Liu, J. Bai, S. Huang, H. Li, X. Chen, *ACS Appl. Mater. Interfaces* **2021**, *13*, 24747.

[49] H. Gommans, B. Verreet, B. P. Rand, R. Muller, J. Poortmans, P. Heremans, J. Genoe, *Adv. Funct. Mater.* **2008**, *18*, 3686.

[50] J. Li, X. Huang, J. Yuan, K. Lu, W. Yue, W. Ma, *Org. Electron.* **2013**, *14*, 2164.

[51] T. Liu, L. Sun, C. Xie, W. Wang, F. Qin, Y. Zhou, *J. Mater. Chem. A* **2021**, *9*, 23269.

[52] J. Zhao, Y. Li, G. Yang, K. Jiang, H. Lin, H. Ade, W. Ma, H. Yan, *Nat. Energy* **2016**, *1*, 15027.

[53] S. R. Cowan, A. Roy, A. J. Heeger, *Phys. Rev. B* **2010**, *82*, 245207.

[54] L. J. A. Koster, V. D. Mihailetchi, R. Ramaker, P. W. M. Blom, *Appl. Phys. Lett.* **2005**, *86*, 123509.

[55] N. Zarrabi, O. J. Sandberg, S. Zeiske, W. Li, D. B. Riley, P. Meredith, A. Armin, *Nat. Commun.* **2021**, *12*, 207.

[56] T. Kirchartz, J. Nelson, *Phys. Rev. B* **2012**, *86*, 165201.

[57] S. Wheeler, F. Deledalle, N. Tokmoldin, T. Kirchartz, J. Nelson, J. R. Durrant, *Phys. Rev. Appl.* **2015**, *4*, 024020.

[58] O. J. Sandberg, A. Sundqvist, M. Nyman, R. Österbacka, *Phys. Rev. Appl.* **2016**, *5*, 044005.

[59] M. Burgelman, P. Nollet, S. Degrave, *Thin Solid Films* **2000**, *361*, 527.

[60] S. Wilken, O. J. Sandberg, D. Scheunemann, R. Österbacka, *Sol. RRL* **2020**, *4*, 1900505.

[61] X. Ma, R. A. J. Janssen, G. H. Gelinck, *Adv. Mater. Technol.* **2023**, *8*, 2300234.

**ADVANCED
SCIENCE NEWS**

www.advancedsciencenews.com

**ADVANCED
MATERIALS**

www.advmat.de

[62] M. Nyman, O. J. Sandberg, W. Li, S. Zeiske, R. Kerremans, P. Meredith, A. Armin, *Sol. RRL* **2021**, *5*, 2100018.

[63] W. Li, S. Zeiske, O. J. Sandberg, D. B. Riley, P. Meredith, A. Armin, *Energy Environ. Sci.* **2021**, *14*, 6484.

[64] O. J. Sandberg, M. Nyman, R. Österbacka, *Phys. Rev. Appl.* **2014**, *1*, 024003.

[65] D. Scheunemann, S. Wilken, O. J. Sandberg, R. Österbacka, M. Schiek, *Phys. Rev. Appl.* **2019**, *11*, 054090.

[66] S. Solak, P. W. Blom, G. Wetzelaer, *Appl. Phys. Lett.* **2016**, 109, 053302.

[67] P. Hang, J. Xie, C. Kan, B. Li, Y. Zhang, P. Gao, D. Yang, X. Yu, *Adv. Mater.* **2021**, *33*, 2006910.